Laser-dressed photoionization for the temporal characterization of attosecond pulses generated from plasma mirrors

L. Dakroub, T. Sinyakova, D. Cubaynes, C. Bomme, L. Chopineau, G. Garcia, O. Peyrusse, F. Quéré, C. Bourassin-Bouchet, A. Klisnick

To cite this version:

L. Dakroub, T. Sinyakova, D. Cubaynes, C. Bomme, L. Chopineau, et al.. Laser-dressed photoionization for the temporal characterization of attosecond pulses generated from plasma mirrors. The European Physical Journal. Special Topics, 2023, 232 (13), pp.2055-2067. 10.1140/epjs/s11734-023-00817-5 . hal-04256581

HAL Id: hal-04256581
https://cnrs.hal.science/hal-04256581v1

Submitted on 25 Oct 2023

Eur. Phys. J. Spec. Top.
https://doi.org/10.1140/epjs/s11734-023-00817-5

THE EUROPEAN
PHYSICAL JOURNAL
SPECIAL TOPICS

Regular Article

Laser-dressed photoionization for the temporal characterization of attosecond pulses generated from plasma mirrors

L. Dakroub[1], T. Sinyakova[1], D. Cubaynes[1], C. Bomme[2], L. Chopineau[2], G. Garcia[3], O. Peyrusse[4], F. Quéré[2], C. Bourassin-Bouchet[5], and A. Klisnick[1,a]

[1] Faculté Des Sciences, ISMO, CNRS, Université Paris-Saclay, 91405 Orsay Cedex, France
[2] LIDYL, CEA, CNRS, Université Paris-Saclay, CEA Saclay, 91191 Gif-Sur-Yvette Cedex, France
[3] Synchrotron SOLEIL, 91192 Gif Sur Yvette Cedex, France
[4] LP3, Aix-Marseille Université, CNRS, 13288 Marseille, France
[5] LCF, Institut d'Optique Graduate School, CNRS, Université Paris-Saclay, 91127 Palaiseau Cedex, France

Received 22 September 2022 / Accepted 10 March 2023

Abstract We report on the implementation of a laser-dressed photoionization method aimed at measuring the temporal structure of high-order harmonics generated from plasma mirrors at the attosecond timescale. Using numerical simulations, we show that the infrared dressing pulse induces up-down asymmetry on the angular distribution of photoelectrons. Experimentally single-shot photoelectron spectra with angular resolution were successfully detected with a velocity-map imaging spectrometer. However, the impact of the infrared dressing field in the photoelectron spectra could not be observed. We discuss several issues that potentially hampered these observations and suggest corresponding setup improvements.

1 Introduction

The recent emergence of intense ultrashort radiation sources in the extreme ultraviolet (XUV) spectral range, namely free-electron lasers [1, 2], high-order harmonics (HH) generated from gases [3, 4] or from plasma mirrors [4, 5], and seeded XUV lasers generated from hot plasmas [6, 7], drives an important effort to develop reliable, accurate, and versatile tools to characterize their main properties. In particular, the question of the temporal pulse structure and duration is of outmost importance. It is an essential piece of information for a better understanding of the underlying physics of the source. It is also required for a proper interpretation of experiments involving their interaction with solid, plasma or gaseous matter in the linear and nonlinear regime, at ultrashort, picosecond to attosecond timescales.

In parallel with the development of these sources, innovative instrumentation and methods adapted to their specific characteristics have been developed and implemented. Considerable progress has been notably achieved for attosecond pulses based on high-order harmonic generation (HH) from gas [8] and for femtosecond XUV and X-ray free-electron lasers [9, 10] in both the self-amplification of spontaneous emission (SASE) mode or seeded mode. Among the different techniques which have been considered for temporal characterization, those based on photoionization of atoms by the XUV pulse in a laser-dressing field have become the most extensively explored, both theoretically and experimentally. This approach consists in focusing the XUV pulse to be characterized along with the dressing field into a gas jet, inducing two-color ionization of the (usually noble-gas) atoms in the volume of interaction. Measuring the kinetic energy distribution of the photoelectrons released in the presence of the dressing field then allows one to recover the temporal structure of the XUV pulse.

For attosecond pulses based on HH generated from gas, different variants of this concept have led to several well-established methods: the Reconstruction of Attosecond Beatings By Interference of Two-photon transitions (RABBIT) [11], attosecond streaking [12], or Frequency-Resolved Optical Gating for Complete Reconstruction of Attosecond Bursts (FROG-CRAB) [13]. For XUV free-electron lasers involving fs to as pulses, THz streaking [14, 15] and techniques based on

---

[a] e-mail: annie.klisnick@universite-paris-saclay.fr (corresponding author)

infrared (IR) laser dressing [16, 17] have been successfully implemented.

Compared to these attosecond pulse sources, high-order harmonics generated from plasma mirrors offer the potential of a large number of photons per pulse at a high photon energy, with a table-top setup [18]. However, their temporal properties have remained largely unexplored, mainly due to their low repetition rate and shot-to-shot fluctuations making these studies challenging. The first attempt to directly measure the temporal structure of the harmonic emission from plasma mirrors was reported in 2009 by Nomura [19] and discussed in deeper details in [20]. The measurement was based on XUV autocorrelation using two-photon ionization of helium as the non-linear process. By detecting the generated He^+ ions as a function of the delay between two replicas of the XUV pulse, evidence of sub-femtosecond structures in the XUV emission was demonstrated. More recently, some of the authors of the present paper (F.Q., L.C., LYDIL, France) reported an all-optical measurement technique, based on dynamical ptychography, from which a temporal width of ˜ 500 as was deduced [21]. Other all-optical techniques were proposed and discussed in [22, 23] but not experimentally attempted, to the best of our knowledge.

In this paper, we discuss the possibility to use laser-dressed photoionization for the temporal characterization of HH generated from plasma mirrors. Compared to HH generated from gas, not only odd but also even harmonics are generated in the emitted XUV pulse. As a result, harmonics and sidebands are no longer well separated, as in the RABBIT process, but instead overlap with each other, making their observation and characterization more challenging. In Sect. 2, using numerical simulations, based on the widely used strong-field approximation, we show how the temporal structure of the XUV pulse could be encoded in the angle-resolved laser-dressed photoelectron spectra. In Sect. 3, we describe the experimental implementation of the method with a particular emphasis on the specific beamlines developed for the IR dressing beam and the XUV harmonic beam. The angular resolution required for the measurement of the laser-dressed photoionization spectra was obtained with a velocity-map imaging spectrometer. Finally in Sect. 4, we present the obtained experimental results. As the impact of the dressing pulse could not be observed in the obtained photoelectron spectra, we discuss potential reasons and suggest several setup improvements, hoping that sharing the experience will benefit future experiments.

2 Laser-dressed photoionization using harmonics generated from plasma mirrors

Generating HH from a plasma mirror in a controlled way requires two successive steps. First, an intense prepulse with a duration of a few tens of fs is focused on a solid target and creates a dense plasma on its surface. At the femtosecond timescale, plasma expansion is very limited during the interaction. An extremely steep plasma interface with vacuum is formed that acts as a mirror for a second ultrashort pulse with an intensity in the 10^{16}–10^{20} W/cm^2 range. Due to the laser/plasma interaction, part of the pulse energy is converted to generate HH of the driving laser frequency in the XUV spectral range. As the interaction medium is not centrosymmetric, the obtained HH spectrum consists of both odd and even harmonics. The emission of these HH can be explained through two dominant generation mechanisms [5]: Coherent Wake Emission (CWE) and the Relativistic Oscillating Mirror (ROM) process. In the CWE mechanism, the driving laser (intensities from 10^{16} to 10^{18} W/cm^2) periodically pulls out and pushes back electrons in the plasma. Doing so, they trigger collective oscillations of electrons in their wake, which in turn emit XUV light. The CWE spectrum usually consists of an harmonic comb ranging from order 2 of the driving laser frequency to a maximum order (typically 15–30), which increases with the plasma electron density. At higher intensities, up to 10^{20} W/cm^2, the electrons oscillate at the plasma surface with relativistic velocities. This plasma then behaves as an oscillating mirror giving rise to a periodic Doppler shift of the reflected beam that takes the form of HH of the incident frequency. Both CWE and ROM can contribute to the harmonic signal, and their relative weight depends notably on the controlled scale length of the plasma density gradient, as well as on the laser intensity (Fig. 1).

In the time domain, this XUV radiation theoretically takes the form of a train of attosecond pulses [5]. To characterize the time structure of these HH, we have chosen to rely on the physical phenomenon called laser-dressed photoionization. The principle consists in measuring the momentum distribution of the photoelectrons freed by the XUV pulse in the presence of an external laser pulse called the dressing field synchronized with the XUV pulse. The spectral phase information, essential for a complete temporal reconstruction of the XUV pulse, is encoded in the photoelectron spectrum through the influence of this dressing pulse.

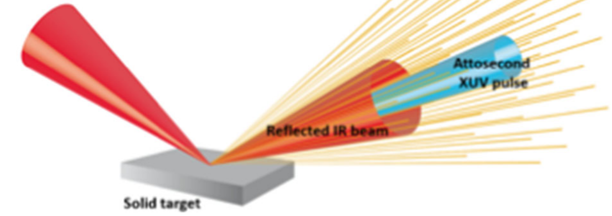

Fig. 1 Schematic representation of the generation of XUV HH radiation from the interaction of ultra-intense laser pulse with a surface plasma

Within the strong-field approximation [24], the photoelectron spectrum $S(\mathbf{p})$ is given in atomic units by:

$$S(\overrightarrow{p}) = \left| \int_{-\infty}^{+\infty} \overrightarrow{d}_{\overrightarrow{p}+\overrightarrow{A}(t)} \cdot \overrightarrow{E}_{\mathrm{XUV}}(t-\tau) e^{i\phi(t)} \mathrm{d}t \right|^2 \tag{1}$$

with $\mathbf{p}$ the final photoelectron momentum, $\mathbf{d}$ the dipole matrix element for the transition from the atomic ground state to the state $\mathbf{p}$ in the continuum, $\mathbf{E}_{\mathrm{XUV}}$ (t) the XUV electric field, $\mathbf{A}$(t) the dressing laser vector potential, and τ the laser/XUV delay. The phase φ(t) accumulated by an electron freed at time t in the laser field is given by the quasi-classical action:

$$\phi(t) = \left[\frac{|\vec{p}|^2}{2} + I_{\mathrm{p}} \right] t - \int_t^{+\infty} \frac{2|\vec{p}| \cdot \left|\vec{A}(t')\right| \cdot \cos\theta + \left|\vec{A}\right|^2 (t')}{2} \mathrm{d}t' \tag{2}$$

with θ the angle between the laser polarization axis and the direction of emission of the photoelectron, and I_{p} the ionization potential of the gas. In historical techniques, such as RABBIT or FROG-CRAB, the spectral phase information is encoded in a two-dimensional trace showing the evolution of the photoelectron spectrum with τ. Changing the delay implies repeating the measurement with another XUV pulse. In the present case, we ultimately seek obtaining as much information as possible on the XUV pulse in a single-shot, taking advantage of the angular distribution of the photoelectrons. When photoionization occurs, electrons are emitted in all directions, forming an expanding sphere of photoelectrons. According to Eq. (2), the influence of the laser-dressing field on these electrons can be split in two contributions: (1) the ponderomotive term in A^2 induces a small shift in energy on the photoelectrons that is independent of their direction of emission; (2) the second term in $p{\cdot}A{\cdot}\cos\theta$ has potentially a much stronger influence on the electron spectrum and varies with θ.

In other words, if a photoelectron is emitted perpendicularly to the laser polarization axis ($\theta = \pm\pi/2$), it will feel only a weak ponderomotive shift. So, we can consider that measuring its energy spectrum in this direction will provide the laser-free spectrum. As θ tends toward zero, the influence of the laser-dressing pulse will become stronger. Measuring the photoelectron kinetic energy distribution in various directions, therefore, amounts to scanning the laser intensity, which encodes the XUV spectral phase. As opposed to the regular laser/XUV delay scan, such an angular scan could be acquired in one shot using a velocity-map imaging spectrometer (VMIS), which provides angle-resolved photoelectron spectra. Even if used in combination with a delay scan, this instrument is particularly suited for the present problem as will be illustrated from the numerical simulations presented below.

Figure 2 shows the influence of the IR dressing field on the angle-resolved photoelectron spectra, calculated from numerical simulations based on Eqs. (1) and (2). The ionizing XUV field is composed of harmonics H11 to H16 of the fundamental IR field ($h\nu_{\mathrm{IR}} = 1.55$ eV), with a zero spectral phase. The target gas is argon ($I_{\mathrm{p}} = 15.76$ eV). For the photoelectron angular distribution, contained in the dipole matrix element of Eq. (1), an asymmetry parameter β with a typical value of 0.5 was used, as obtained from an average of the published data over the considered photon energy range (17–25 eV) [25]. The dressing field consists of a gaussian pulse with a duration of 30 fs full-width at half maximum (FWHM), a central photon energy of 1.55 eV (corresponding to a period $T_0 = 2.67$ fs), a zero spectral phase and a field intensity of 4 TW/cm^2. Both XUV and IR fields are linearly polarized in the same direction shown by the purple (Fig. 2a) and red (Fig. 2b) arrows, respectively.

In Fig. 2a, only the XUV ionizing pulse is present. The photoelectron spectrum is composed of six concentric rings, the radius of which equals the square root of the electron kinetic energy E_{k} for each harmonic ($E_{\mathrm{k}}(q) = \times\ 1.55 - I_{\mathrm{p}}$, for $q \in$ [11–16]). The modulation of the spectrum in the presence of the IR dressing field is shown in Fig. 2b, c for two different XUV–IR delays, $\tau_1 = T_0/4 = 0.67$ fs and $\tau_2 = 3\ T_0/4 = 2.0$ fs, respectively. For each spectrum, the left half of the panel shows the projected 3D distribution of the sphere of photoelectrons, while the right half shows the retrieved 2D distribution of the central slice. For both delays, the dressing field induces a strong up-down asymmetry, albeit with opposite directions.

Figure 2d shows that this asymmetry effect would still be visible after integrating angularly the top and bottom parts in the retrieved central slice for each delay. The case without dressing field is also shown (grey peaks in Fig. 2d). For both delays, all harmonic peaks are slightly shifted ($\Delta E_{\mathrm{pond}} = 0.24$ eV) toward lower kinetic energies through the ponderomotive effect. For a delay of $\tau_1 = T_0/4 = 0.67$ fs, the intensity of the higher energy peaks is stronger for the bottom-part integrated spectrum (in blue), while it is weaker for the top-part integrated spectrum (in red). At a larger delay of $\tau_2 = 3\ T_0/4 = 2.0$ fs, the opposite trend is observed.

We note that a similar up-down asymmetry effect in the photoelectron angular distribution was previously reported and discussed by Loriot et al. [26], while using an HH XUV source generated from a rare gas as the ionizing pulse and the second harmonic of the fundamental laser as the dressing pulse. As in our case, such a configuration results in the superposition of the dressing-induced sidebands of the neighboring harmonic.

Figure 3 shows that, in the presence of the dressing field, the photoelectron spectrum is also sensitive to the spectral phase of the XUV ionizing pulse. In Fig. 3a, the calculated spectrum is obtained for the same XUV and IR pulse parameters as in Fig. 2, but for an intermediate delay $\tau_3 = T_0/2 = 1.34$ fs, for which the temporal peaks of the XUV pulse train coincide with the maxima of the IR dressing field, that is the so-called streaking regime. For this particular delay, one can see that there is no up-down asymmetry when the attosecond XUV

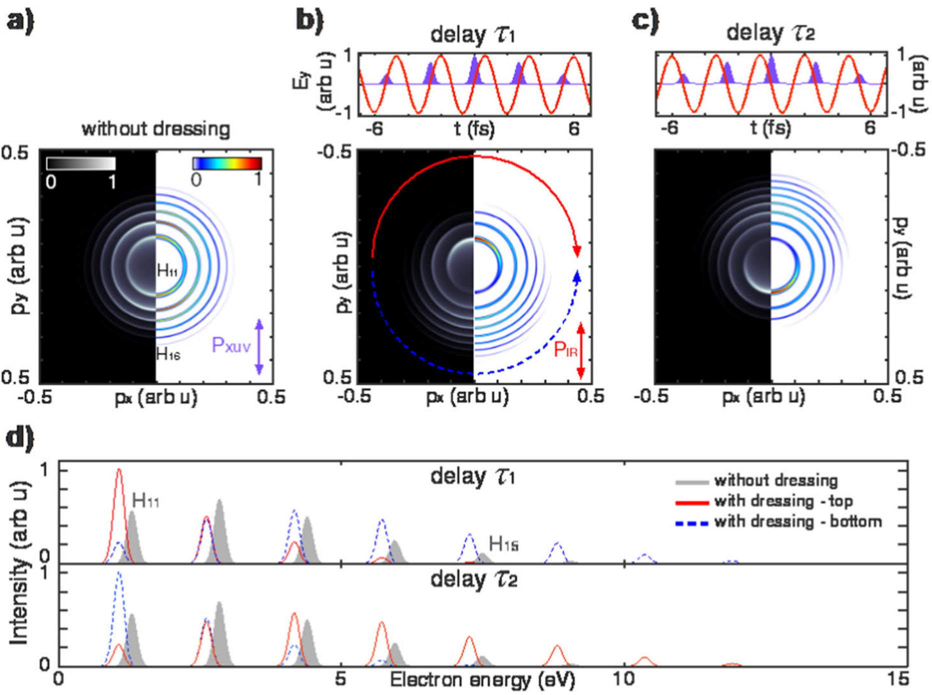

Fig. 2 Calculated angular distribution of the photoelectron momenta (left: projected sphere, right: central slice). **a** Without, dressing field; **b**, **c** with the IR dressing field (4TW/cm^2), for two different IR–XUV delays: $\tau_1 = T_0/4 = 0.67$ fs and $\tau_2 = 3\ T_0/4 = 2.0$ fs. A strong up-down asymmetry is observed for both delays. This asymmetry is still visible in **d** after angularly integrating the top and bottom parts of the retrieved central slice for both delays. Both XUV and IR field are linearly polarized in the vertical direction, as shown by the purple (resp. red) arrow

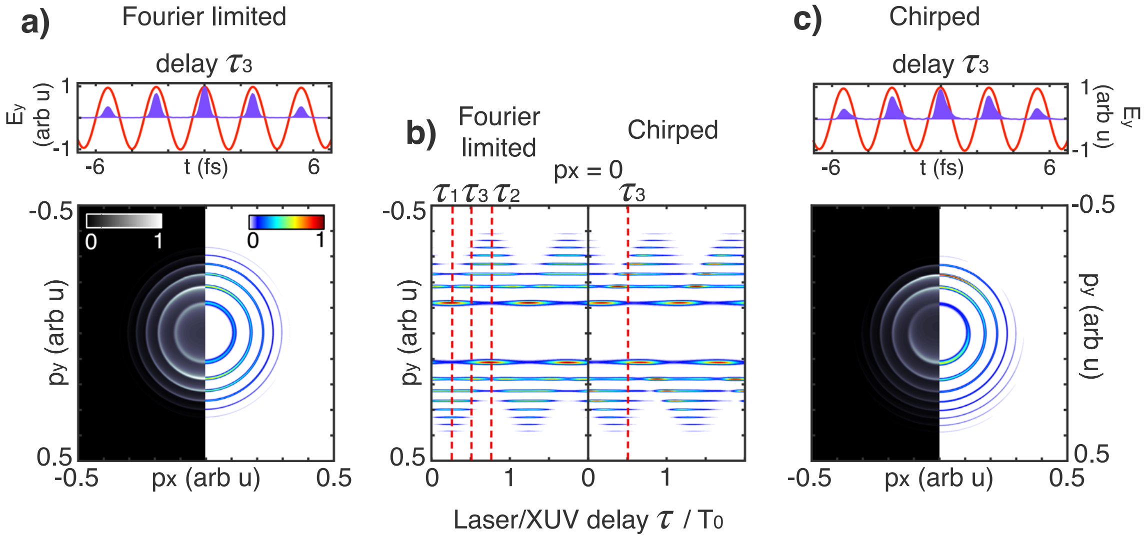

Fig. 3 Calculated angular distribution of the photoelectron momenta (left: projected sphere, right: central slice) at time delay $\tau_3 = T_0/2 = 1.34$ fs. **a** Fourier-limited XUV pulse; **c** chirped XUV pulse. **b** Spectrograms taken at $p_x = 0$ for the Fourier-limited (left) and the chirped (right) XUV pulse

pulses are Fourier-limited. Conversely, a small chirp is introduced in the XUV pulses in Fig. 3c. Although this barely affects their time profile, it is sufficient to introduce a clear up-down asymmetry on the angle-resolved spectrum. This demonstrates the strong sensitivity of this arrangement to the XUV spectral phase.

Finally, Fig. 3b displays the spectrograms composed of the juxtaposition of the central slice spectra at $p_x = 0$, over an XUV–IR delay range of $2 \bullet T_0$ for the Fourier-limited pulse (left) and for the chirped pulse (right). One can see that the up-down asymmetry oscillates with a period that corresponds to the IR laser period T_0. The presence of the chirp slightly distorts the oscillatory trends in the spectrogram compared to the Fourier-limited pulse case.

This numerical example illustrates that the spectral phase, and thus the time structure, of the attosecond pulse train (APT) is fundamentally encoded in the single-shot angular spectrum at delay τ_3. The next step is the extraction of this temporal information from the spectrum, which can be achieved with the help of a phase-retrieval algorithm. Together with the experimental arrangement, the numerical inversion algorithm would form the complete temporal metrology tool. This has proven to be a robust strategy as demonstrated by the historical success of the FROG-CRAB technique, and of more recent variants [16]. The details of this inversion algorithm will be published in an upcoming article. For the sake of completeness, we exemplify briefly its capabilities below. Similarly to FROG-CRAB where both the XUV pulse and the laser gate can be recovered from the spectrogram, this algorithm allows the reconstruction of both the attosecond pulse and the temporal phase ϕ_{pA} defined as:

$$\phi_{\mathrm{pA}}(t) = p_y^{\max} \int_t^{+\infty} A(t')\mathrm{d}t'.$$

This phase corresponds to the momentum-dependent contribution in the phase $\varphi(t)$ given by Eq. (2), where $p_y^{\max}$ is the upper bound of the p_y scale in the VMI image. From $\phi_{\mathrm{pA}}(t)$, it is then possible to obtain the time structure of the dressing pulse electric field, its peak intensity, and its relative synchronization with respect to the XUV pulse during the interaction.

As an illustration, the algorithm is used to process the central slice of the angular distribution at delay τ_3 shown in the right half of Fig. 3a (Fourier limited case) and Fig. 3c (chirped case). After 600 iterations of the Hybrid-Input–Output algorithm followed by 500 iterations of the Error Reduction algorithm [27], the quantities shown in Fig. 4 are reconstructed. The temporal intensity and phase of the APT are properly reconstructed (only the intensity is shown) both in the Fourier-limited case (Fig. 4a) and in the chirped case (Fig. 4b). The phase $\phi_{\mathrm{pA}}(t)$ is also retrieved correctly, its relative timing with respect to the attosecond pulses confirms that the APT is synchronized with an extremum of dressing pulse electric field, as is expected from the interaction at delay τ_3. Finally, this confirms that the angular distribution of photoelectron contains sufficient information to reconstruct quantitatively and unambiguously the temporal structure of the attosecond pulses.

The above numerical study also indicates that the ponderomotive shift of the harmonic peaks and the up-down asymmetry in the angular distribution of photoelectrons are, thus, the two major effects that were expected to be observed in the VMI spectra obtained in the experimental campaign described below.

3 Experimental implementation

The experiment was performed at the UHI100 laser facility hosted at LIDYL, CEA-Saclay (France). The CPA-based Ti–Sapphire laser system is able to deliver 25 fs pulses with a peak power of 100 TW and a focused intensity up to 10^{20} W/cm^2 on target. A double-plasma mirror device [28] is used to improve the temporal contrast (better then 10^{10}) of the pulse and an adaptive optics system is used to optimize the focal spot by reducing the wavefront aberrations of the laser beam prior to focusing.

3.1 Experimental setup

The temporal characterization of ultrashort XUV pulses using the laser-dressed photoionization technique requires to fulfill three imperative conditions at the position where the measurement is made: (1) temporal synchronization of the IR and XUV pulses with accurate control of their relative delay at the IR subcycle timescale; (2) spatial overlap of the corresponding focal spots, and (3) controlled intensity of IR dressing laser pulse. Applying those challenging constraints to the specificities of the plasma-mirror XUV HH source led us to opt for a full co-propagative beamline design shown in Fig. 5, where the main IR beam, the dressing beam, and the XUV beam are all reflected off the same optical elements. Doing so, one limits the influence of the mechanical instabilities in optical mounts on the IR/XUV delay, while both IR and XUV pulses are naturally overlapped and synchronized into the VMI spectrometer. Importantly, the fact that the IR dressing beam is reflected on the target at the same position where the HH XUV source is generated is a requirement to ensure that the temporal overlap between the both pulses is maintained while the target is refreshed at each shot by translating it along its surface. The other requirement of the designed beamline is to transport both the XUV and the IR dressing beams to the interaction zone in the VMIS, while eliminating the high-intensity IR driving laser beam downwards the target.

After entering the first experimental chamber, the main IR laser beam (diameter 60 mm), which is p-polarized, is split into two parts, using a 5 mm diameter mask (see (2) in Fig. 5) with a central hole (variable diameter 1.75, 2.75, and 3.4 mm). This leads to an annular driving beam for the generation of the XUV HH source and a central dressing beam with a variable diameter. A 1/2″ mirror (not shown in Fig. 5), placed at a variable distance in front of mirror (1) and close to its outer edge, is used to generate a low-energy prepulse with a controlled delay [16]. Mirror (1) was manufactured with a step in its center to delay the outer part of the beam relative to the central part (see bottom inset in Fig. 5), so as to compensate for the delay acquired by the dressing beam when traversing the CaF$_2$ plate (3) and the bandpass filter (9). The CaF$_2$ plate can be slightly tilted to allow a fine adjustment and a controlled variation of the delay between the driving and dressing pulses (see top inset in Fig. 5). Both driving and dressing beams are then focused with 45∘ incidence angle onto the SiO$_2$ solid target (5) with the help of an off-axis parabola (f = 304 mm) (4).

An iris (6) was then used to block the reflected annular IR beam while transmitting the produced high-order harmonic XUV beam. A 100 nm thick, mesh-supported aluminum filter (7) was used to filter out any remaining scattered IR light, while a 5 mm hole in the filter allowed the transmission of the central laser-dressing

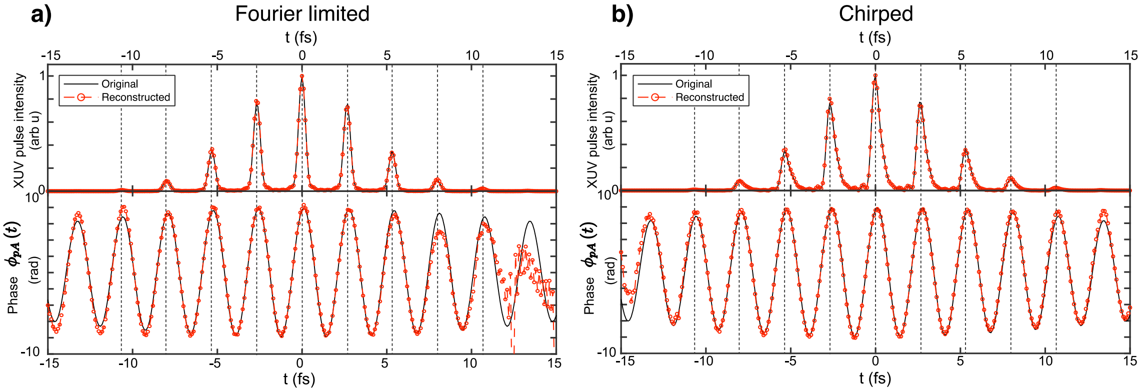

Fig. 4 Reconstruction of attosecond pulse trains from the angular distribution of photoelectrons in the case of **a** Fourier-transform limited XUV pulses and **b** chirped XUV pulses. Only the intensity (squared modulus) of the attosecond pulses is shown. In the lower panels, the phase $\phi_{\mathrm{pA}}(t)$ is shown. In each panel, the black continuous curve and the red dashed line with circles indicate the exact quantity and the reconstructed one, respectively. The vertical dotted lines highlight the relative synchronization between the attosecond pulse train and the dressing pulse electric field at the moment of the interaction in the gas jet

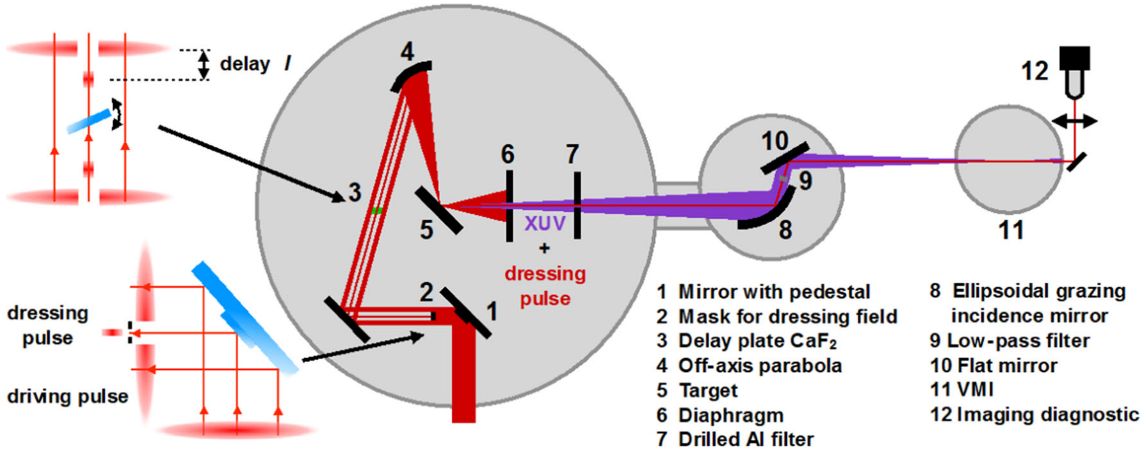

Fig. 5 Experimental setup showing the IR (red) and XUV (purple) beamlines. Insets: (bottom) generation of an annular driving laser beam and a central dressing beam; (top) the delay of the dressing pulse relative to the driving pulse is controlled by slightly tilting the $\mathrm{CaF_2}$ plate

beam. The transmission of the Al filter was of typically 0.7–0.8 for harmonics orders $11 < q < 16$.

A flat-field XUV spectrometer (not shown in Fig. 5) could be inserted in the beam path to optimize the XUV harmonic emission spectrum with respect to the main driving parameters, notably the delay between the prepulse and the main pulse. For the photoelectron spectra measurements, the XUV beam and the IR dressing beam were sent to a second vacuum chamber in which they were reflected under 11.5° grazing incidence by a combination of an ellipsoidal mirror (8) with $f = 1$ m and a flat mirror (10), both made of fused silica with a 40 nm Au surface coating. The ellipsoidal mirror imaged the target surface position where the IR (main and dressing) beams are focused and the XUV harmonic emission is generated. A $2f$–$2f$ configuration (magnification $M = 1$) was used to minimize aberrations. Since the IR dressing beam and the generated XUV harmonics beam originate from the same position at the target, they are naturally overlapped in space and synchronized in time (or delayed by a controlled amount) at the image plane. Both focii were accurately positioned at the center of the VMIS interaction zone, using tilt adjustment with the planar mirror. Additional controls of the position and relative timing of the beams focal spots in the interaction zone are described in Sect. 3.3.

Finally, to filter out the lowest harmonic orders and to avoid their potential contribution to the dressing field, a 5 mm diameter longpass filter (9) was accurately positioned between the two grazing incidence mirrors on the path of the central IR beam dressing beam, thus also intercepting a small central part of the XUV beam.

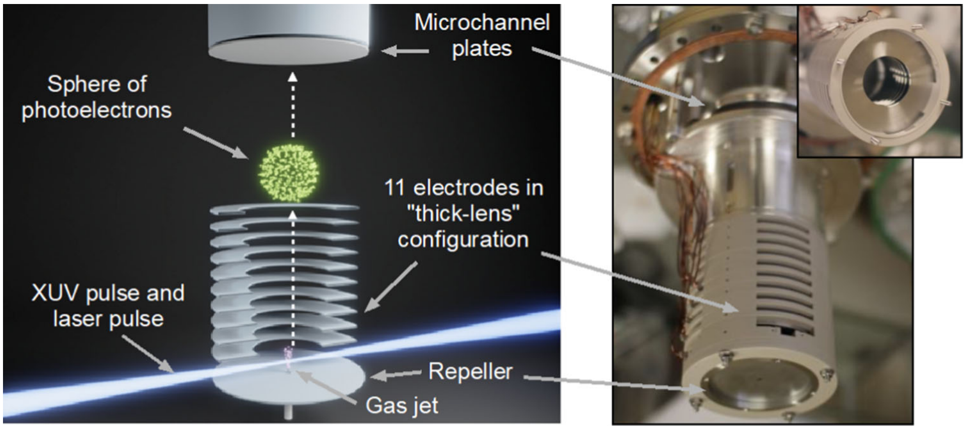

Fig. 6 Schematic (left) and photo (right) of the velocity-map imaging spectrometer

3.2 Velocity-map imaging (VMI) spectrometer

Our VMI spectrometer (see Fig. 6), designed and built at ISMO (Orsay, France), includes a 11 electrode assembly mounted in a "thick lens" configuration [29]. This configuration was shown to maintain a good energy resolution over a broad kinetic energy range $E_\mathrm{k} \sim 0$ to 100 eV. The XUV beam and the IR dressing beam were focused into a gas jet placed between the repeller and the extractor electrodes of the VMIS, as schematically shown in Fig. 6. The gas is injected by a polarized needle going through a 3 mm hole in the repeller. When photoionization occurs in the gas jet, the sphere of photoelectrons is projected by the intense electrostatic field onto a position sensitive detector, providing an image of the photoelectrons angular distribution. The detector is composed of a single microchannel plate (MCP), or a stack of two MCPs of 80 mm diameter, coupled to a P43 phosphor screen, which is finally imaged by a cooled CCD camera.

This instrument was designed to become a mobile diagnostic that can be mounted on existing XUV beamlines to characterize the temporal properties of their pulses. The VMI spectrometer was commissioned prior to the experiment with two different XUV sources: a cw-helium discharge lamp with photon energy of 21.21 eV, and a pulsed plasma-based XUV laser with photon energy of 38 eV (LASERIX facility, IJC-Lab, Université Paris-Saclay). The energy resolution ΔE/E measured for the kinetic energy region E_k between 5 and 23 eV was typically of 4% (FWHM). The calibration curve of the VMIS was also obtained, relating the outer radius R of the projected sphere of photoelectrons to its kinetic energy E_k, for different values of the repeller voltage V_rep. The measured data were found to fit well with the expected VMI calibration law: $E_\mathrm{k}/V_\mathrm{rep} = R^2/C^2$ [30], yielding a value of $C = 25.9$ cm for the VMI constant.

For alignment purpose, which will be further discussed in Sect. 3.3, the VMI spectrometer was also operated in the spatial map imaging mode (SMI). In this mode, the image of the interaction zone is obtained by projecting the photoions on the detector plane with a positive electrostatic field. For a ratio $V_\mathrm{rep}/V_\mathrm{ext} = 0.95$ (V_ext is the voltage applied to the extractor), numerical simulations performed using the SIMION code with our electrode geometry predict a spatial magnification of 1 in the center of the image.

3.3 Control of the XUV and dressing beams in the VMIS

An optical imaging system including a CCD detector, see (12) in Fig. 5, was positioned at the VMI exit port to obtain a magnified image of the IR laser focal spot at the position of the interaction region inside the VMIS. During the measurement part of the experiment, it was used either to monitor shot-by-shot the size and position of the focused dressing beam, or to check that no IR beam was incident in the interaction zone when the dressing beam was blocked. For the alignment part of the experiment, the aluminium filter being temporarily removed, the imaging system was used to control the spatial overlap between the main IR beam and the dressing beam, as well as their precise temporal overlap and relative delay by observing the position of their interference fringes. With this technique, it was estimated that the relative delay could be controlled with an accuracy of the order of 100 as. It should be noted that the spatial and temporal overlap of the XUV and IR pulses using this method relies on the assumption that the main IR pulse and the XUV harmonic pulse perfectly coincide both in time and space in the interaction zone, with the required accuracy (namely 10 µm and 10 fs). This will be further discussed in the last part of the paper.

Using the VMI spectrometer in the SMI mode, the transverse position of the focii for the XUV ionizing pulse and the IR dressing pulse, with respect to the gas jet in the interaction region, was adjusted by tilting the grazing incidence planar mirror. Figure 7 shows an example of an image obtained in a single shot when the XUV beam alone was sent into the gas jet. The bright zone of the signal corresponds to the intersection of the focused beam with the gas jet, while the weaker signal on each side is due to the ionization of the lower density residual gas in the spectrometer ($p = 10^{-5}$ mbar).

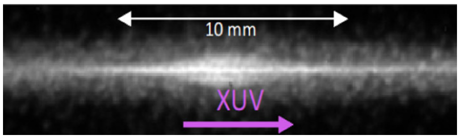

Fig. 7 Single-shot detector image in the spatial map imaging mode using the XUV beam (direction of propagation shown by the purple arrow) focused in the Ar gas jet

Figure 8 displays single-shot detector images obtained in the SMI mode when only the IR dressing beam was sent into the VMIS. The intensity of the focused IR beam was varied between 2 TW/cm^2 and 90 TW/cm^2, by adjusting both the incident laser energy and the diameter of the hole in mask (2) (Fig. 5). To evaluate the intensity, a calorimeter positioned at the output port of the VMIS was used to measure the IR transmitted energy, while (in a subsequent shot) the diameter of the IR focal spot was obtained from the IR optical imaging system. One can see in Fig. 8 that the presence of traces of ionization of the gas target is observed for intensities above ˜ 20 TW/cm^2. This is consistent with the typical minimum intensity (˜ 10 TW/cm^2) required to achieve above-threshold ionization (ATI) processes with a 800 nm laser pulse. This result was used to assess that more than sufficient intensity was available to induce laser-dressed photoionization processes in our experiment.

4 4. Experimental results and discussion

4.1 Without dressing

First, using the XUV flat-field spectrometer, the delay between the prepulse and the main pulse was adjusted so as to optimize the generated HH spectrum in the ROM regime [31]. Then the XUV beam was sent into the interaction zone of the VMIS to ionize the gas target. We used two rare gases with different ionisation potential I_{p} and asymmetry parameter β: argon with $I_{\mathrm{p}} = 15.76$ eV and β ranging from 0.1 to 1 in the [17–25] eV photon energy range [25]; and neon with $I_{\mathrm{p}} = 21.56$ eV and β ranging from $-$ 0.5 to 0.3 in the [23–30] eV photon energy range [32].

Figure 9 displays single-shot detector images obtained in the velocity-map imaging mode showing the projection of the photoelectron angular distribution generated from argon (Fig. 9a), and neon (Fig. 9b). In each panel, the left image is the raw projected sphere, while the right image shows the 2D distribution of the central slice retrieved from inverse-Abel transformation with the pBasex algorithm [33], taking the direction of polarization of the XUV harmonics radiation as the symmetry axis. In both images, one can clearly observe the concentric rings corresponding to photoionization by the successive high-order harmonics at kinetic energies $E_{\mathrm{k}}(q) = q \times 1.55 - I_{\mathrm{p}}$, with q being the harmonic (odd and even) order.

Another interesting feature, which can be seen in the inversed spectra (right image in Fig. 9a, b), is that the angular distribution of photoelectrons varies with the HH order and with the target gas. The observed variation is qualitatively consistent with the corresponding values of the asymmetry parameter β available from the literature [25, 32] for single-photon ionization by a linearly polarized XUV radiation. For example, in argon (Fig. 9a), the angular distribution is almost uniform for H11 ($h\nu = 17$ eV, $\beta = 0.1$), while it is more peaked in the polarization direction (see purple arrow) for HH15 ($h\nu = 23.2$ eV, $\beta = 1.1$). In neon, the angular distribution at the HH15 photoline is slightly peaked in the horizontal (perpendicular to polarization) direction ($h\nu$ = 23.2 eV, $\beta = -$ 0.5), while it is almost uniform for

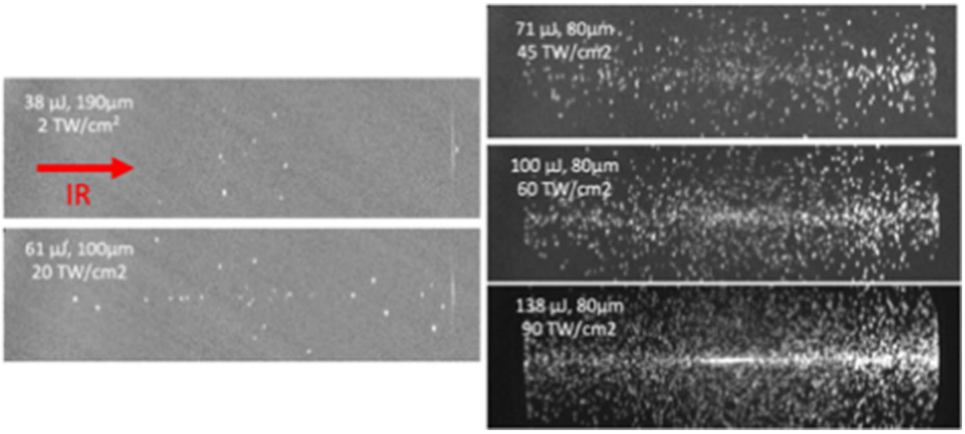

Fig. 8 Single-shot detector images of photoions obtained in the spatial map imaging mode using the IR dressing laser beam only (direction of propagation shown by the red arrow), at increasing values of focused intensity. In each image, the values of the measured IR transmitted energy and focal spot diameter are indicated along with the corresponding focused intensity. Traces of photoionization start to be observed when the IR intensity is above 20 TW/cm^2, as expected from ATI processes

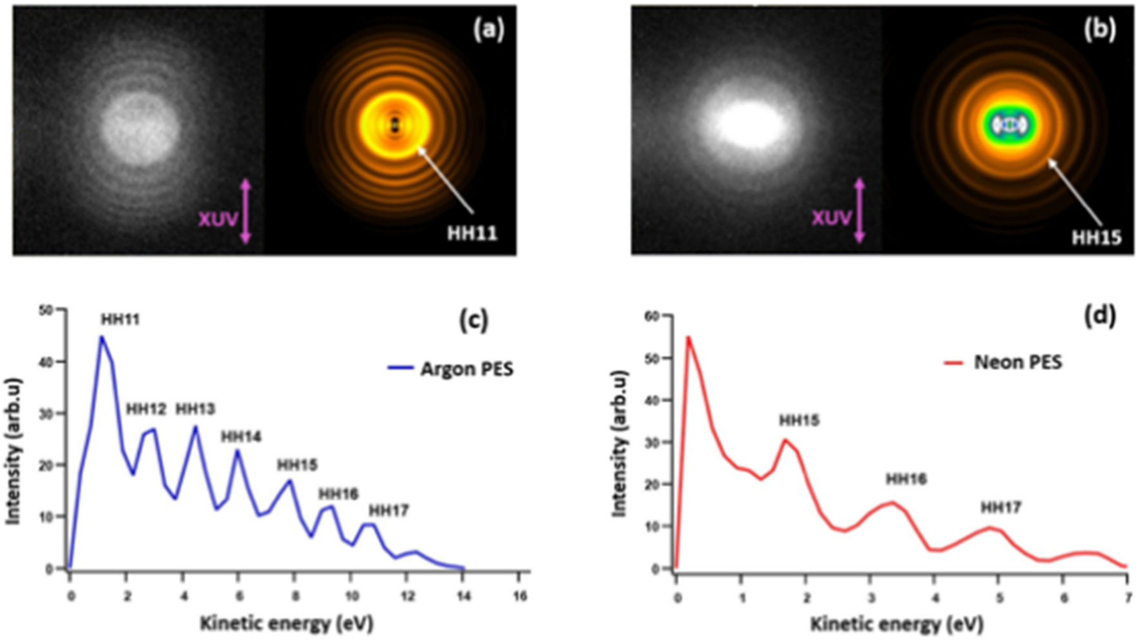

Fig. 9 Single-shot experimental VMI images obtained in argon (**a**) and neon (**b**). In each panel, the left image shows the raw spectrum and the right image is the retrieved central slice of the sphere of photoelectrons using the pBasex inversion software, taking the XUV polarization direction (purple arrow) as the symmetry axis. The concentric rings correspond to the successive orders of the HH pulse, while the lowest observed order is indicated by an arrow. **c**, **d** Angularly integrated photoelectron spectra obtained from the inverted images

the HH17 photoline ($h\nu = 26.3$ eV, $\beta = 0$). We mention, however, that the measured β values were found to be systematically smaller by a factor ˜ 2 compared to the corresponding values from the literature. This discrepancy is not fully understood yet. We believe that it could be due to the contribution of photoionization by unpolarized thermal incoherent plasma emission, which will be discussed further in Sect. 4.

Remarkably, the experimental images presented in Fig. 9 were obtained in single shot. Single-shot photoelectron spectra obtained from a relativistic plasma surface XUV source were first reported by Heissler et al. [34], using a magnetic-bottle electron spectrometer. Here, we show that angular distributions can also be obtained in a single shot, using a VMI spectrometer, which represents an achievement in itself.

4.2 With dressing

Photoelectron spectra were then obtained with both the XUV pulse and the IR dressing pulse focused in the VMIS, while varying their relative delay over a period with ˜ 500 as steps. The IR intensity at focus was of the order of 20 TW/cm^2. According to the simulations presented in Figs. 2 and 3, this should in principle lead to an unambiguous influence of the dressing pulse on the photoelectrons angular distribution. Examples of obtained experimental images without and with IR dressing are shown in Fig. 10. The left panels show the raw detector images (averaged over 3 shots), while the right panels show the spectra after angularly integrating the top and bottom parts of the retrieved central slice, without IR laser (top), and with dressing laser for 5 different XUV–IR delays ranging between 0 and 0.8 $T_0 = 2.14$ fs. One can see that no evidence of up-down asymmetry is observed at any delay. More surprisingly, we do not observe any ponderomotive shift of the photolines toward lower momenta, whereas the expected shift ($\Delta E_{\text{pond}} = 1.2$ eV for $I = 20$ TW/cm^2 at l = 800 nm) is significant compared to the separation between two successive harmonics ($\Delta E = 1.55$ eV). A second delay scan was also achieved at a lower IR dressing intensity of 9 TW/cm^2, which did not reveal any effect of the laser-dressing field.

4.3 Discussion

In this section, we review the potential reasons that could explain the absence of any observable impact of the dressing field in the photoelectron spectra. We then suggest several setup improvements for future experiments. Especially as mentioned earlier, the technique of laser-dressed photoionization demands to fulfill three important practical conditions: (1) temporal overlap of the XUV and dressing pulses, (2) spatial overlap of the XUV and dressing beams in the VMI interaction region, and (3) control of the dressing pulse intensity.

Regarding condition (3), the energy of the dressing pulse was measured with a calorimeter at the output flange of the VMIS. It proved to be more than sufficient in theory to induce a visible impact on the spectra. This

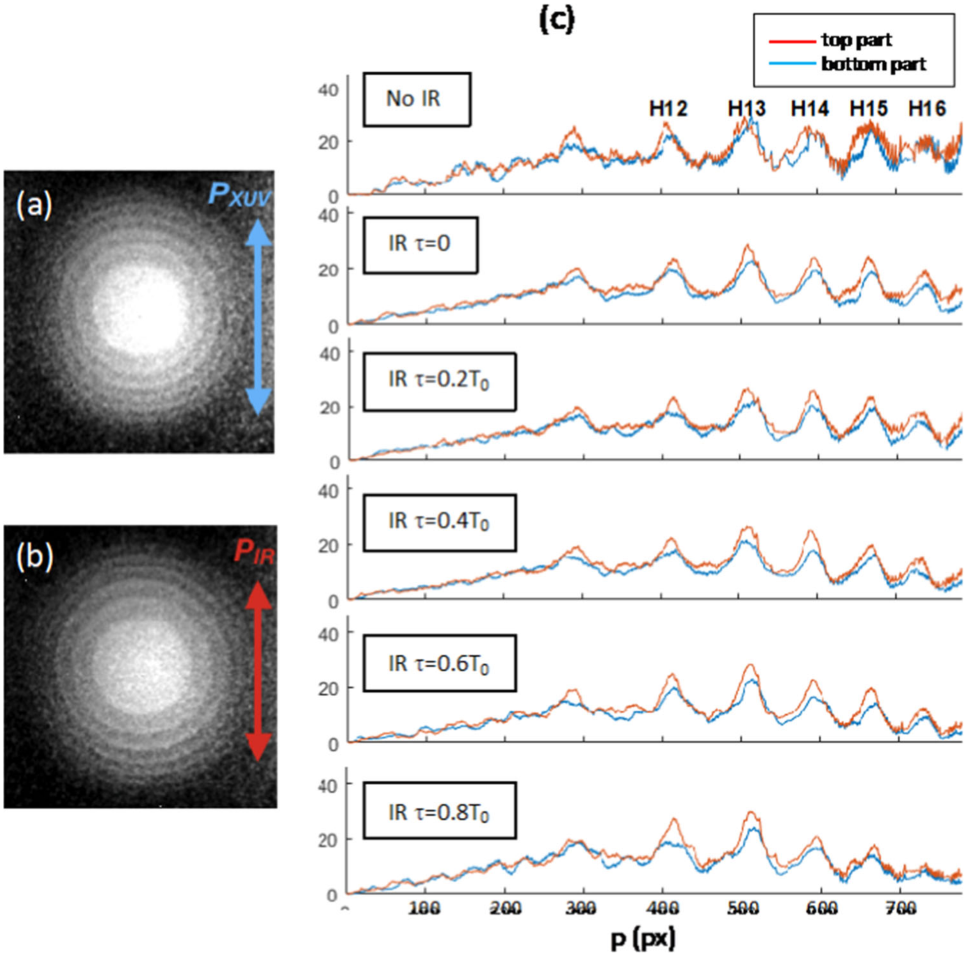

Fig. 10 Experimental VMI image (averaged over three shots) **a** without and **b** with IR dressing laser ($I_{\text{IR}} = 2 \bullet 10^{13}$ W/cm^2) in argon gas. After inversion, each half image is averaged angularly, resulting in the red and blue spectra in **c** where p denotes the radial moment. No evidence of a laser-dressing effect is observed in the spectra obtained at different XUV–IR delays, compared to the case without IR laser shown at the top

was confirmed by the observation of above-threshold ionization (ATI) as mentioned before. The spatial overlap condition was in principle guaranteed by our setup. The imaging of the VMI interaction region also seemed to confirm that the spatial overlap condition was fulfilled, see Figs. 7, 8.

We estimate that temporal overlap was the most critical condition to achieve and maintain. Interference fringes were observed when overlapping the driving and dressing beams after the VMI near the zero delay. This, however, does not ensure that the IR dressing pulse and the XUV pulse could remain synchronized until they reach the VMI. If the two pulses experience slightly different beam paths (with lengths differing by more than a few microns), this might vary their relative delay by a few tens of fs. Such desynchronization would be sufficient to lose the temporal overlap, which would prevent any modulation of the photoelectron spectrum by the dressing pulse. Moreover, optical path distortions can also cause transverse variations of the dressing-XUV delay across the beam. Indeed, given the large divergence of plasma-mirror harmonics, it is certain that the XUV beam illuminated almost entirely the ellipsoidal grazing incidence mirror. In these conditions, misalignments or surface defects of the mirror can rapidly cause spatio-temporal stretching of attosecond and femtosecond pulses upon reflection [35, 36]. Therefore, even if the temporal overlap could be maintained, such transverse delay variations would wash out the spectrograms shown in Fig. 3, preventing from observing variations of the photoelectron spectrum with the delay.

To diagnose the presence of such optical path distortions in our experiment, we opened the iris and removed the Al filter (elements 6 and 7 in Fig. 5) to illuminate almost completely the ellipsoidal mirror with the main IR laser beam, and we imaged the focal spot obtained in the VMI. In our setup, this 500-mm-focal-length mirror was used to refocus the XUV source in the VMI with a magnification of 1. When perfectly aligned, this optical geometry should lead to a diffraction-limited focal spot. However, the obtained spot turns out to be slightly asymmetric, a bounce is present on one side of the spot, see Fig. 11a, b. This suggests the presence of residual coma aberration, which could be explained by an effective magnification slightly different from 1. This was confirmed by simulating this focusing geometry using the numerical code described in Ref. [35]. When decreasing the magnification down to 0.98, simulations reproduce very well the bounce observed in the focal spot. Moreover, this magnification corresponds to

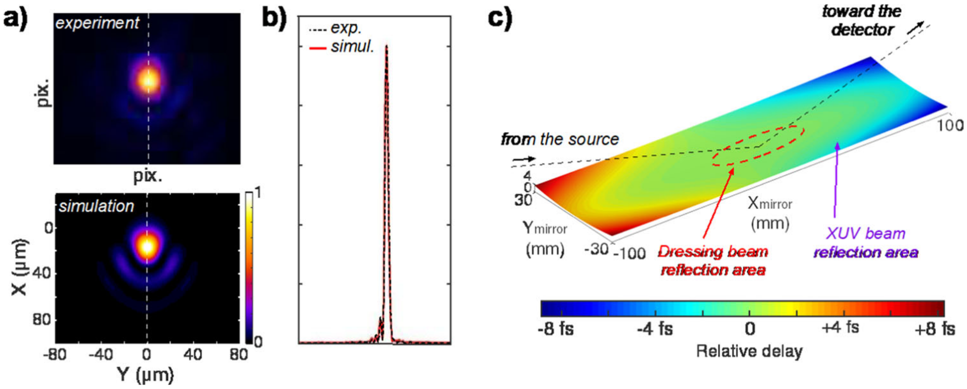

Fig. 11 **a** Measured (top) and simulated (bottom) focal spot for the IR beam illuminating the ellipsoidal mirror completely. The experimental image is well reproduced while assuming a magnification of 0.98 instead of 1. **b** Lineout along the dotted line in **a**. **c** Relative delays accumulated by optical rays as a function of their point of reflection on the mirror. The shaded area shows the dressing beam reflection area when the Al filter and iris limit are in place

deviations of the source-mirror and mirror-focus distances of $\sim$ 1 cm over 1 m, which is within the alignment accuracy. Although apparently negligible, these residual aberrations lead to significant delays at the femtosecond timescale. Figure 11c shows the relative delays accumulated by optical rays as a function of their point of reflection on the ellipsoidal mirror. These delays are computed for rays emitted by a HH source point and reaching the paraxial focal plane in the VMI interaction region.

When the magnification is 1, no delay occurs between the rays and the beam remains diffraction limited. For a magnification of 0.98 as described in Fig. 11, the accumulated delay can reach ± 8 fs at the edges of the mirror with respect to its center. In the grey-shaded area representing the area of reflection of the dressing beam, the delay range is restricted to ± 1 fs. We estimate that the ± 8 fs delay range obtained in simulations is a best-case scenario. Indeed, we emphasize that these simulations do not account for the surface's defects due to imperfect manufacturing, which were yet present. These defects can increase further this delay range without necessarily having a strong impact on the IR focal spot. Additionally, we here considered one of the nicest IR focal spot. In practice, it was observed that the spot could vary on a shot-to-shot basis in the experiment. Finally, while an accurate control of the reproducibility of the XUV beam pointing and of its far-field intensity profile was achieved with the same source in the experiment reported in [21], significant shot-to-shot variations were observed in our experiment, likely due to the added complexity of the conditions of HH generation.

Although indirect, this semi-quantitative study does suggest the presence of optical path distortions strong enough to degrade the dressing-XUV temporal overlap in our experiment. Therefore, we consider that such effects should be treated seriously in future experiments, for instance by utilizing careful optical alignment procedures combined with imaging at focus of the XUV beam or XUV wavefront characterization.

Although not as critical as the temporal overlap condition, we estimate that thermal plasma emission might have played a detrimental role in the experiment. As the plasma is driven by the intense femtosecond laser pulse, high harmonics are produced. At longer timescales, the expanding plasma then emits continuum and line radiation over a broad energy range. Figure 12a shows the emission spectrum from a dense, highly ionized Si plasma as calculated from a collisional-radiative code [37]. The plasma electron density N_e and temperature T_e values considered in this calculation are taken from a 1D-hydrocode simulation using laser parameters similar to the experimental ones. They correspond to the position where the maximum temperature is reached soon after the interaction with the main driving pulse. One can see that strong line emission is visible up to 2.5 keV.

Figure 12b shows the calculated overall transmission of the XUV beamline used in our experiment, using reflection and transmission values from tabulated data. One can see that photons energies above ˜ 200 eV are efficiently suppressed by the two Au-coated mirrors, as they do not satisfy the total-reflection condition at grazing incidence. However, it turns out that plasma emission below 200 eV is not sufficiently filtered out and is, therefore, transmitted to the VMIS where it can significantly contribute to the photoelectron signal. Indeed, the spectral lines in this energy range belong to various Si ionic species between Si^{11+} and Si^{4+} [38]. These ions will, thus, emit not only close to the maximum of the plasma temperature, close to the peak of the main laser pulse, but also on a much longer time after the laser interaction during the plasma cooling and recombination phase. These high photon energies will photoionize the gas jet in the VMIS and produce photoelectron spheres with large radii which, when projected onto the detector, will build up an intense noise background on the VMI images. Such a background was actually observed in our experimental images, in particular in shots where the emission of high-order harmonics was intentionally supressed by adjusting the prepulse level.

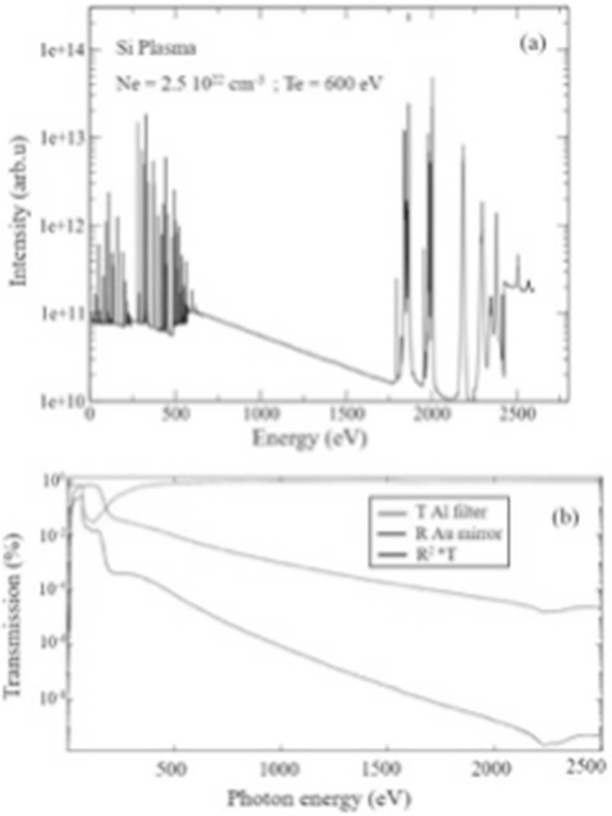

Fig. 12 **a** Emission spectrum in the [0–2500 eV] range calculated for a Si plasma at N_e = 2.5•10^{22} cm^{-3} and T_e = 600 eV. These plasma conditions were calculated from a 1D-hydrosimulation using laser parameters similar to the experimental ones. **b** Overall transmission (black) of the XUV beamline including reflection (blue) from the ellipsoidal and flat mirrors and transmission (red) through the Al filter

To filter out the unwanted contribution of thermal plasma emission, we, thus, recommend to adopt further filtration of the ionizing radiation, for example, using extra metallic filters, and to gate the high voltage of the micro-channel plates to restrict the signal contributions to the narrow time window of the high-harmonics.

5 Conclusion

In conclusion, we have presented what we believe to be the first and yet almost unique experimental attempt to implement a laser-dressed photoionization technique to high-order harmonics generated from plasma mirrors, with the aim of characterizing its temporal structure at the attosecond timescale. Numerical simulations show that the IR dressing field should induce an up-down asymmetry in the angular distribution of photoelectrons, oscillating at the IR field period with respect to the delay between the XUV and IR pulses.

Using a home-made velocity-map imaging spectrometer, angular photoelectrons distributions were successfully measured in argon and neon in a single XUV shot. However, in spite of a carefully designed beamline to transport and focus both the IR and the XUV beams to the VMIS interaction zone with high spatial and temporal accuracy, the influence of the laser-dressing pulse could not be observed in the photoelectron spectra. We discuss two main potential reasons, namely the mixing of delays in the interaction zone due to residual aberration in the beam foci, and the contribution of thermal plasma emission to the photoelectron signal. Although they do not completely explain the absence of any observable laser-dressing impact in our detected VMI spectra, they definitely contribute to hamper the targeted, yet challenging, measurement of oscillation of an up-down asymmetry in the spectrogram. Finally, we suggested several setup improvements that should be included in future experiments.

Funding This project has received funding from Labex PALM (ANR-10-LABX-0039-PALM), LIDEX OPT2X, Sesame PULSE- X, Laserlab-Europe (EU-H2020 871124). We gratefully acknowledge helpful discussions with L. Nahon (SOLEIL Synchrotron) as well as the invaluable support of engineers and technicians, in particular J. Guigand, C. Charrière, N. Tournier at ISMO, and F. Réau, P. d'Oliveira at CEA-LIDYL.

Data availability The datasets generated during and/or analyzed during the current study are available from the corresponding author on reasonable request. This manuscript has associated data in a data repository. [Authors' comment: The raw data reported in this study are available from the corresponding author on reasonable request.]

References

1. W. Ackermann, G. Asova, V. Ayvazyan et al., Nat. Photon. **1**, 336–342 (2007)
2. E. Allaria, C. Callegari, D. Cocco, W.M. Fawley, M. Kiskinova, C. Masciovecchio, F. Parmigiani, New J. Phys. **12**, 075002 (2010)
3. P. Corkum, F. Krausz, Nat. Phys. **3**, 381–387 (2007)
4. S. Chatziathanasiou, S. Kahaly, E. Skantzakis, G. Sansone, R. Lopez-Martens, S. Haessler, P. Tzallas, Photonics **4**, 26–65 (2017)
5. C. Thaury, F. Quéré, J. Phys. B At. Mol. Opt. Phys. **43**, 213001 (2010)
6. Y. Wang, E. Granados, F. Pedaci, D. Alessi, B. Luther, M. Berrill, J.J. Rocca, Nat. Photon. **2**, 94–98 (2018)
7. A. Depresseux, E. Oliva, J. Gautier, F. Tissandier, J. Nejdl, M. Kozlova, S. Sebban, Nat. Photon. **9**, 1–6 (2015)
8. I. Orfanos, I. Makos, I. Liontos, E. Skantzakis, B. Förg, D. Charalambidis, P. Tzallas, APL Photon. **4**, 5086773 (2019)
9. S. Düsterer, M. Rehders, A. Al-Shemmary, C. Behrens, G. Brenner, O. Brovko, S. Schreiber, Phys. Rev. Spec. Top. Acceler. Beams **17**, 120702 (2014)

10. W. Helml, I. Grguraš, P.N. Juranić, S. Düsterer, T. Mazza, A.R. Maier, R. Kienberger, Appl. Sci. (Switzerland) **7**, 1–42 (2017)
11. P.M. Paul, E.S. Toma, P. Breger, G. Mullot, F. Auge, P. Balcou, H.G. Muller, P. Agostini, Science **292**, 1689 (2001)
12. E. Goulielmakis, M. Uiberacker, R. Kienberger, A. Baltuska, V. Yakovlev, A. Scrinzi, T. Westerwalbesloh, U. Kleineberg, U. Heinzmann, M. Drescher, F. Krausz, Science **305**, 1267 (2004)
13. Y. Mairesse, F. Quéré, Phys. Rev. A **71**, 011401(R) (2005)
14. U. Frühling, M. Wieland, M. Gensch, T. Gebert, B. Schütte, M. Krikunova, R. Kalms, F. Budzyn, O. Grimm, J. Rossbach, E. Plönjes, M. Drescher, Nat. Photon. **3**, 523 (2009)
15. R. Ivanov, I.J.B. Macias, J. Liu, G. Brenner, J. Roensch-Schulenburg, G. Kurdi, U. Frühling, K. Wenig, S. Walther, A. Dimitriou, M. Drescher, I.P. Sazhina, A.K. Kazansky, N.M. Kabachnik, S. Düsterer, J. Phys. B At. Mol. Opt. Phys. **53**, 184004 (2020)
16. N. Hartmann, G. Hartmann, R. Heider, M.S. Wagner, M. Ilchen, J. Buck, A.O. Lindahl, C. Benko, J. Grünert, J. Krzywinski et al., Nat. Photon. **12**, 215 (2018)
17. P.K. Maroju, C. Grazioli, M. Di Fraia, M. Moioli, D. Ertel, H. Ahmadi, O. Plekan, P. Finetti, E. Allaria, L. Giannessi, G. De Ninno, C. Spezzani et al., Nature **578**, 386 (2020)
18. J. Bierbach, C. Rödel, M. Yeung, B. Dromey, T. Hahn, A.G. Pour, S. Fuchs, A.E. Paz, S. Herzer, S. Kuschel, O. Jäckel, M.C. Kaluza, G. Pretzler, M. Zepf, G.G. Paulus, New J. Phys. **14**, 065005 (2012)
19. Y. Nomura, R. Hörlein, P. Tzallas, B. Dromey, S. Rykovanov, Z. Major, J. Osterhoff, S. Karsch, L. Veisz, M. Zepf, D. Charalambidis, F. Krausz, G.D. Tsakiris, Nat. Phys. **5**, 124 (2009)
20. R. Hörlein, Y. Nomura, P. Tzallas, S.G. Rykovanov, B. Dromey, J. Osterhoff, Z. Major, S. Karsch, L. Veisz, M. Zepf, D. Charalambidis, F. Krausz, G.D. Tsakiris, New J. Phys. **12**, 043020 (2010)
21. L. Chopineau, A. Denoeud, A. Leblanc, E. Porat, P. Martin, H. Vincenti, F. Quéré, Nat. Phys. **17**, 968 (2021)
22. F. Quéré, H. George, Ph. Martin, Proc. SPIE **7359**, 73590E (2009)
23. C. Wu, L. Li, M. Yeung, S. Wu, S. Cousens, S. Tietze, B. Dromey, C. Zhou, S. Ruan, M. Zepf, Opt. Express **30**, 389–402 (2022)
24. K. Varjú, P. Johnsson, J. Mauritsson, T. Remetter, T. Ruchon, Y. Ni, F. Lépine, M. Kling, J. Khan, K.J. Schafer, M.J.J. Vrakking, A. L'Huillier, J. Phys. B At. Mol. Opt. Phys. **39**, 3983 (2006)
25. D.M.P. Holland et al., Nucl. Instrum. Methods **195**, 331–337 (1982)
26. V. Loriot, A. Marciniak, G. Karras, B. Schindler, G. Renois-Predelus, I. Compagnon, B. Concina, R. Brédy, G. Celep, C. Bordas, E. Constant, F. Lépine, J. Opt. (UK) **19**, 114003 (2017)
27. J.R. Fienup, Appl. Opt. **21**, 2758–2769 (1982)
28. A. Lévy, T. Ceccotti, P. D'Oliveira, F. Réau, M. Perdrix, F. Quéré, P. Monot, M. Bougeard, H. Lagadec, P. Martin, J.-P. Geindre, P. Audebert, Opt. Lett. **32**, 310 (2007)
29. N.G. Kling, D. Paul, A. Gura, G. Laurent, S. De, H. Li, Z. Wang, B. Ahn, C.H. Kim, T.K. Kim, I.V. Litvinyuk, C.L. Cocke, I. Ben-Itzhak, D. Kim, M.F. Kling, J. Instrum. **9**, P0505 (2014)
30. G.A. Garcia, L. Nahon, C.J. Harding, E.A. Mikajlo, I. Powis, Rev. Sci. Instrum. **76**, 053302 (2005)
31. S. Kahaly, S. Monchocé, H. Vincenti, T. Dzelzainis, B. Dromey, M. Zepf, Ph. Martin, F. Quéré, Phys. Rev. Lett. **110**, 175001 (2013)
32. K. Codling, R.G. Houlgate, J.B. West, P.R. Woodruff, J. Phys. B **9**, L83 (1976)
33. G.A. Garcia, L. Nahon, L. Powis, Rev. Sci. Instrum. **75**, 4989 (2004)
34. S. Heissler, P. Tzallas, J.M. Mikhailova, K. Khrennikov, L. Waldecker, F. Krausz, S. Karsch, D. Charalambidis, G.D. Tsakiris, New J. Phys. **14**, 043025 (2012)
35. C. Bourassin-Bouchet, S. de Rossi, F. Delmotte, P. Chavel, J. Opt. Soc. Am. A **27**, 1395 (2010)
36. C. Bourassin-Bouchet, M. Mang, F. Delmotte, P. Chavel, S. de Rossi, Opt. Express **21**, 2506–2520 (2013)
37. O. Peyrusse, M. Busquet, J.C. Kieffer, Z. Jiang, C.Y. Côté, Phys. Rev. Lett. **75**, 3862 (1995)
38. NIST Atomic Spectra Database. https://www.nist.gov/pml/atomic-spectra-database. Accessed May 2022